Surface-Regulated Nano-SnO₂/Pt₃Co/C Cathode Catalysts for Polymer Electrolyte Fuel Cells Fabricated by a Selective Electrochemical Sn Deposition Method

Kensaku Nagasawa,[†] Shinobu Takao,[†] Shin-ichi Nagamatsu,[†] Gabor Samjeské,[†] Oki Sekizawa,[†] Takuma Kaneko,[†] Kotaro Higashi,[†] Takashi Yamamoto,[§] Tomoya Uruga,[†,∥] and Yasuhiro Iwasawa*[†,‡]

[†]Innovation Research Center for Fuel Cells and [‡]Graduate School of Information Science Engineering, The University of Electro-Communications, Chofugaoka, Chofu, Tokyo 182-8585, Japan

[§]Faculty for Integrated Arts and Sciences, The University of Tokushima, Minamijosanjima, Tokushima 770-8502, Japan

[∥]Japan Synchrotron Radiation Research Institute, SPring-8, Sayo, Hyogo 679-5198, Japan

Ⓢ *Supporting Information*

ABSTRACT: We have achieved significant improvements for the oxygen reduction reaction activity and durability with new SnO₂-nanoislands/Pt₃Co/C catalysts in 0.1 M HClO₄, which were regulated by a strategic fabrication using a new selective electrochemical Sn deposition method. The nano-SnO₂/Pt₃Co/C catalysts with Pt/Sn = 4/1, 9/1, 11/1, and 15/1 were characterized by STEM-EDS, XRD, XRF, XPS, in situ XAFS, and electrochemical measurements to have a Pt₃Co core/Pt skeleton-skin structure decorated with SnO₂ nanoislands at the compressive Pt surface with the defects and dislocations. The high performances of nano-SnO₂/Pt₃Co/C originate from efficient electronic modification of the Pt skin surface (site 1) by both the Co of the Pt₃Co core and surface nano-SnO₂ and more from the unique property of the periphery sites of the SnO₂ nanoislands at the compressive Pt skeleton-skin surface (more active site 2), which were much more active than expected from the d-band center values. The white line peak intensity of the nano-SnO₂/Pt₃Co/C revealed no hysteresis in the potential up−down operations between 0.4 and 1.0 V versus RHE, unlike the cases of Pt/C and Pt₃Co/C, resulting in the high ORR performance. Here we report development of a new class of cathode catalysts with two different active sites for next-generation polymer electrolyte fuel cells.
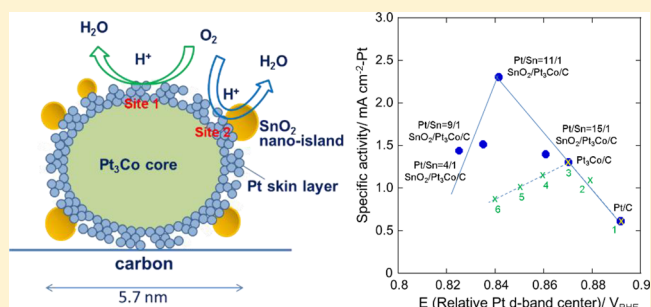
■ INTRODUCTION

Development of next-generation polymer electrolyte fuel cells (PEFCs) with high performance and durable cathode catalysts under harsh PEFC operating conditions is indispensable for widespread commercialization of PEFC vehicles.[1−7] Various sorts of Pt−M alloys/C have been studied as one of the most promising candidates as cathode catalysts, and many efforts have been devoted to fabrication of Pt−Co nanostructures with higher oxygen reduction reaction (ORR) activity and longer-term durability than Pt/C, although alloy nanoparticles are indicated to be unstable in acidic environments.[8−23] The Co additive effects on Pt/C have also been characterized by, for example, transmission electron microscopy (TEM),[16,24−28] in situ time-resolved and spatially resolved X-ray absorption fine structure (XAFS),[29−33] and theoretical calculations.[34−36] In contrast, Pt/C cathode catalysts have been modified by metal oxides such as SnOₓ,[37−40] MoOₓ,[41] CeOₓ,[42] TiOₓ,[43] and Ti₀.₇Mo₀.₃O₂[44] to change the redox behavior and improve ORR activity of Pt nanoparticles. The CeOₓ additives were indicated to suppress Pt oxide formation and mitigate Pt particle aggregation though CeOₓ with basic surface character dissolutes into acidic media.[42] The Ti₀.₇Mo₀.₃O₂ mixed oxide was shown to promote the ORR activity of Pt/C by electron transfer from the oxide to Pt.[44]

Recently, we found better ORR performance with a SnO₂-modified Pt₃Sn/C cathode catalyst than with a Pt/C catalyst, where the SnO₂/Pt₃Sn/C catalyst was prepared by reduction of a Pt−Sn/C sample with H₂ at 573 K to form Pt₃Sn alloy/C, followed by oxidation with O₂ at 573 K to form SnO₂ islands at the surface.[37−40] However, this method cannot be applied to fabrications of other SnO₂/Pt−M alloys/C because it is hard to segregate only SnO₂ islands at the surface of Pt−Sn−M ternary alloys on carbon. Here, we report a new way to fabricate surface-regulated SnO₂/Pt₃Co/C cathode catalysts with SnO₂ nanoislands on the Pt skeleton-skin surface with compressive strain and defects/dislocations on Pt₃Co nanoparticle cores, which were much more active than expected from the d-band center values. The structural arrangement created two different reaction sites (site 1 at the Pt skin surface and the more active site 2 at the nano-SnO₂ periphery) in a tunable mode with different Pt/Sn ratios, resulting in much more ORR activity and

durability than that of Pt/C catalyst at rotating disk electrodes (RDE) in 0.1 M $HClO_4$.

■ EXPERIMENTAL SECTION

Preparation of $SnO_2/Pt_3Co/C$ Catalysts. A given amount (0.144, 0.086, or 0.062 g) of $SnCl_2$ was dissolved in 0.1 M $HClO_4$ aqueous solution (100 mL), to which 1 g of Pt_3Co/C was added and suspended under stirring. After stirring for 30 min, the potential of −0.45 V vs Ag/AgCl was applied to the solution for 5 days. After filtration of the solution, the obtained sample was washed with 50 mL of ultrapure water (Milli-Q water, Milli-Q Co.) 15 times, followed by drying at 313 K under vacuum for 2 days and subsequent gentle oxidation with O_2 at room temperature for 1 day to form SnO_2 nanoislands. SnO_2 is stable without significant dissolution in the acidic media.[45]

A Pt/C catalyst with a Pt particle size similar to that of the Pt_3Co particle size of the Pt_3Co/C catalyst (TEC36E52, Tanaka Kikinzoku Kogyo) was also prepared for comparison. Commercial Pt/C (TEC10E50E, Tanaka Kikinzoku Kogyo) with 2.5–3.0 nm Pt nanoparticles was heated from room temperature to 823 K at a heating rate of 4.2 K min^{-1} and kept at 823 K for 2 h in a flow of N_2 at 5 mL min^{-1}.

Characterizations. XAFS measurements at Pt L_{III}-edge and Sn K-edge for the $SnO_2/Pt_3Co/C$ catalysts were conducted using Si(111) and Si(311) double-crystal monochromators, respectively, in a fluorescence mode using ion chambers (I_0: Ar 15%/N_2 85% for Pt L_{III} edge and Ar 75%/ Kr 25% for Sn K-edge; I_f: Ar 70%/N_2 30% for Pt L_{III}-edge and Kr 100% for Sn K-edge) for incident and fluorescent X-rays at BL01B1and BL40XU stations, respectively, (for powder samples). In situ Pt L_{III}-edge, Co K-edge, and Sn K-edge XAFS at rotating disk electrodes (RDE) in 0.1 M $HClO_4$ were measured by using a 21 Ge-elements detector at BL36XU station in SPring-8. X-ray absorption near-edge structure (XANES) spectra were normalized by Athena software.[46] The XAFS spectra were treated with the data analysis program IFEFFIT (version 1.2.11c).[47] Theoretical phase and amplitude functions were calculated from FEFF 8.20.[48]

A field-emission transmission electron microscope (FE-TEM, JEM-2100F, JEOL) equipped with an energy dispersive spectrometer (EDS) was used for line scans and point spectra of the catalyst nanoparticles. The FE-TEM was operated at 200 kV in the scanning mode. For TEM observation, samples were dispersed in acetone by sonication, placed on carbon film deposited on Cu grids (200 mesh and 3 mm diameter), and dried. The average particle size was estimated from more than 200 particles.

XRD patterns for $SnO_2/Pt_3Co/C$, Pt_3Co/C, and Pt/C were measured by RINT2000 (Rigaku) with Cu Kα radiation generated at 40 kV and 40 mA in the 2θ range of 10−90° and at a step scan speed of 0.02°/s. XRF measurements were carried out on a ZSX Primus2 (Rigaku) using a Rh X-ray tube at 60 kV/50 mA. Quantifications of Pt, Co, and Sn were carried out by making their standard curves.

The oxidation states of Pt and Sn in the catalysts were estimated from Pt 4f and Sn 3d binding energies in the XPS spectra (JPS-9200, JEOL) using Mg Kα radiation at 10 kV and 10 mA as an excitation source. The Co 2p XPS spectra were also measured to examine if they are located in/near the surface layers. The XPS binding energies were referred to that of C 1s in a graphitic state (284.5 eV).

Electrochemical Measurements. The electrochemical properties of the catalysts were measured at RDE in 0.1 M $HClO_4$ by using 10 μL of a mixture of absolute ethanol (1750 μL), ultra pure water (750 μL), 5% Nafion solution (25 μL), and catalyst powder (4.4 μg-Pt cm^{-2}) deposited on a glassy-carbon (GC) electrode (ϕ = 5 mm) and dried at room temperature in ambient air. The catalysts at the RDE were treated by 50 aging cycles between 0.05–1.2 V vs RHE (V_{RHE}) at 50 mV s^{-1} in N_2-saturated 0.1 M $HClO_4$ solution. Cyclic voltammetries (CV) were recorded between 0.05 and 1.2 V_{RHE} at 50 mV s^{-1} and liner sweep voltammetries (LSV) were recorded from 0.05 to 1.0 V_{RHE} at 10 mV s^{-1}. Accelerated durability tests (ADT) were carried out by rectangular load cycles (up to 5000 cycles) between 0.6 and 1.0 V_{RHE} (6 s for each cycle).

The ORRs at RDE were measured in the AutoLab Potential and Galvanostat system (EcoChemie) with a rotation system of Pine MSR Rotate Assembly Instructions (AFMSRCE series, Pine Instruments). A three-electrode system with a platinum wire as a counter electrode and RHE electrode as a reference electrode was used in the experiments. The electrochemical surface areas (ECSAs) were estimated using the integration of hydrogen absorption and desorption areas in CV curves.[49,50] The ECSA is given by $(Q_{abs} + Q_{des}/2)/(2.1 \times [Pt])$, where Q_{abs} and Q_{des} are electric charges calculated using the potential scan speed and the above enclosed areas, the value 2.1 represents the electric charge per unit surface area (C m^{-2}) of Pt for the hydrogen absorption and desorption, and [Pt] is Pt loading.

CO-Stripping Potentials. After the aging treatment in N_2-saturated 0.1 M $HClO_4$, CO was bubbled for 15 min, then Ar was bubbled for 15 min to remove the dissolved CO in the solution. The CO-stripping potentials were measured in the potential region of 0.05−1.2 V_{RHE} and at a scanning rate of 50 mV/s. It is reported that the higher Pt d-band center energy induces the stronger CO adsorption because of a decrease in the electron back-donation from Pt to the antibonding orbitals of CO molecules.[51] The CO-stripping peak potentials may shift by Pt alloying,[52−55] but the Sn atoms in our catalysts exist as SnO_2. Hence, the CO-stripping peak shift is not due to Pt alloying effect. As a result, the CO-stripping peak potential for the catalysts is regarded to correlate with the Pt d-band center.

■ RESULTS AND DISCUSSION

Fabrication of $SnO_2/Pt_3Co/C$ Catalysts. A series of $SnO_2/Pt_3Co/C$ catalysts with Pt/Sn = 4/1, 9/1, 11/1, and 15/1 were prepared by the selective electrochemical deposition of Sn metal (Sn^0) on Pt_3Co/C (TEC36E52, Tanaka Kikinzoku Kogyo) at −0.45 V vs Ag/AgCl in 0.1 M $HClO_4$. The log j versus potential plots in Figure 1 revealed that the Sn
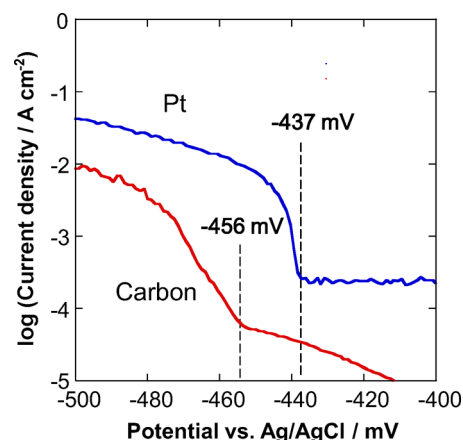

Figure 1. Tafel plots for Pt and carbon working electrodes at 60 s/mV with Ag/AgCl reference electrode in 0.1 M $HClO_4$ solution including 50 mM $SnCl_2$.

deposition on Pt and carbon working electrodes occurred in the potential regions lower than −0.437 and −0.456 V vs Ag/AgCl, respectively. Thus, the best reduction potential for achieving the selective deposition and fast reduction of Sn species on Pt_3Co nanoparticles with Pt-enriched surfaces on carbon in 0.1 M $HClO_4$ was decided to be −0.45 V. At this potential, the Sn^0 deposition predominantly occurs on the Pt surfaces, and the Sn^0 deposition on the carbon can be neglected.

Particle sizes for the as-fabricated $SnO_2/Pt_3Co/C$ (Pt/Sn = 4/1, 9/1, 11/1, and 15/1), Pt_3Co/C, and Pt/C were calculated from XRD patterns using the Scherrer's equation (5.9−6.2 nm) and also estimated by TEM images (5.4−5.7 nm) as shown in

Table 1. Particle Sizes, Metal Loadings, and Their Atomic Ratios in the SnO₂/Pt₃Co/C, Pt₃Co/C, and Pt/C Cathode Catalysts by XRD, TEM, and XRF

samples		particle size (nm)			XRF			
		XRD	TEM[a]	Pt (wt %)	Co (wt %)	Sn (wt %)	Pt/Co[b]	Pt/Sn[b]
SnO₂/Pt₃Co/C	Pt/Sn = 4/1	6.0	5.6	47.0	4.9	7.5	2.9/1.0	3.9/1.0
	Pt/Sn = 9/1	5.9	5.7	47.0	4.9	5.0	2.9/1.0	8.9/1.0
	Pt/Sn = 11/1	6.2	5.6	48.0	5.0	4.0	2.9/1.0	11.1/1.0
	Pt/Sn = 15/1	6.1	5.5	48.0	5.0	1.9	2.9/1.0	15.3/1.0
Pt₃Co/C		6.2	5.4	48.0	5.0	0	2.9/1.0	
Pt/C		6.2	5.4	46.0	0	0		

[a]Average size (±0.7 nm). [b]Atomic ratio.

Table 1 and Figure S1. XRD patterns for the SnO₂/Pt₃Co/C samples identified the Pt₃Co alloy phase with $Pm3m$ space group, similar to the Pt₃Co/C (Figure S2). Neither crystalline Sn⁰ nor SnO₂ phases were involved in all SnO₂/Pt₃Co/C catalysts as shown in the XRD patterns. The white line intensity and feature of the normalized XANES spectra at Sn K-edge for the SnO₂/Pt₃Co/C samples (Pt/Sn = 4/1 and 9/1) coincided with those for SnO₂ (Figure 2), and the XPS binding energies
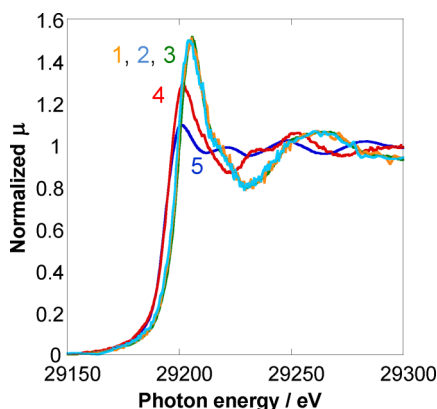

Figure 2. Normalized XANES spectra at the Sn K-edge for SnO₂/Pt₃Co/C (Pt/Sn = 4/1 (orange, 1) and 9/1 (light blue, 2)) and references SnO₂ (green, 3), SnO (red, 4), and Sn (blue, 5).

for Sn 3d₃/₂ and 3d₅/₂ levels (495.2 and 487.1 eV) for the SnO₂/Pt₃Co/C samples were essentially similar to those for SnO₂. No metallic Sn 3d XPS peaks were observed (Figure S3b). These results evidence that the Sn atoms electrochemically deposited on the Pt₃Co nanoparticle surface were oxidized to SnO₂ under O₂ atmosphere at room temperature for 1 day. The binding energies of the Pt 4f₅/₂ and 4f₇/₂ XPS peaks (74.7 and 71.6 eV, respectively) for the Pt₃Co/C shifted by 0.2 eV to the lower binding energies compared to the values 74.9 and 71.8 eV for Pt/C, respectively, demonstrating electron transfer from Co to Pt due to Pt 4f–Co 3d hybridization. The peak top for SnO₂/Pt₃Co/C (Pt/Sn= 9/1 (light blue, 2)) in Figure 2 slightly shifted to the lower energy compared to that for SnO₂, and the white line peak intensity decreased slightly with the SnO₂/Pt₃Co/C (Pt/Sn= 9/1). In contrast, the Sn 3d XPS peak in Figure S3b showed a small peak shift toward higher binding energy with SnO₂/Pt₃Co/C (Pt/Sn = 11/1, 9/1, and 4/1) compared to that of SnO₂. From these controversial data for the bulk-type XANES information and surface-type XPS information, we propose that the Sn atoms of SnO₂ nanoislands at the interface with the Pt skeleton surface layer may be in a oxidation state slightly lower than +4.0 because of oxygen

defects, whereas the other Sn atoms of SnO₂ nanoislands may be in a oxidation state slightly higher than +4.0 because of electron transfer to the Pt skeleton surface layer, showing electronic interaction of the SnO₂ nanoislands with the Pt surface. Further discussion on this issue would not be valid without further evidence at moment, which is beyond the aim of this study.

Figure 3a,b shows a TEM image for the as-fabricated SnO₂/Pt₃Co/C catalyst with Pt/Sn = 9/1 and EDS line profiles for Pt,
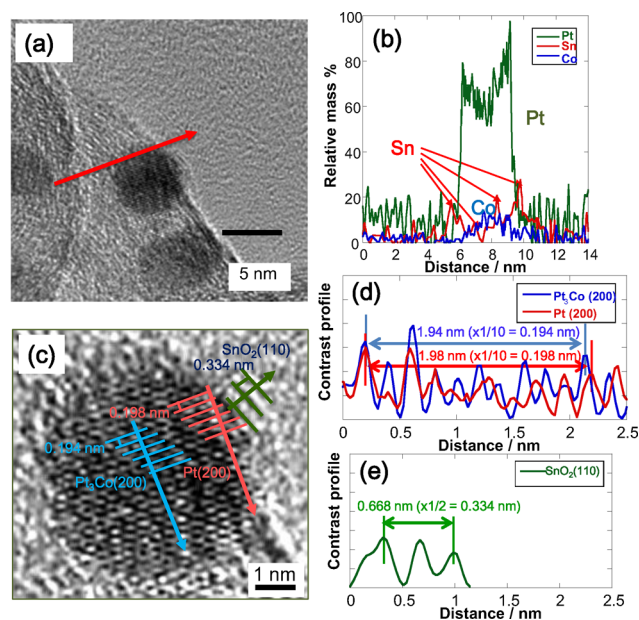

Figure 3. (a) TEM image of the as-fabricated SnO₂/Pt₃Co/C catalyst (Pt/Sn = 9/1) and (b) EDS line profiles for Pt (green), Sn (red), and Co (blue) along the red arrow of a. (c) HR-TEM image of SnO₂/Pt₃Co/C (Pt/Sn = 9/1) and spacings of the lattice planes assigned to Pt₃Co(200), Pt(200), and SnO₂(110) planes. (d) Lattice contrast profiles of the Pt₃Co(200) and Pt(200) directions and (e) of the SnO₂(110) direction.

Sn, and Co along the red arrow in Figure 3a, respectively. The EDS line analysis revealed a Pt-enriched surface, which is partially covered by SnO₂ nanoislands. The Co signal in the EDS profile was negligible near the surface. XPS Co 2p signals in Figure S4 were not detected for all the SnO₂/Pt₃Co/C samples (Pt/Sn = 11/1, 9/1, and 4/1) as well as the Pt₃CO/C sample, which also augments the fact of Pt-enriched-surface nanoparticles. In the SnO₂/Pt₃Co/C prepared by the selective electrochemical Sn deposition method, all SnO₂ species observed by TEM were located on the nanoparticles. In general, adhesion of transition metal oxides on carbon induces

depression of the electrical conductivity of the carbon. Hence, the selective nano-SnO_2 decoration on the Pt-enriched-surface nanoparticles provides a significant advantage as a cathode catalyst.

Figure 3c shows an HR-TEM image of the $SnO_2/Pt_3Co/C$ (Pt/Sn = 9/1) and spacings of the lattice planes assigned to $Pt_3Co(200)$, Pt(200), and $SnO_2(110)$ planes, and Figure 3d,e shows the lattice contrast profiles of the $Pt_3Co(200)$ and Pt(200) directions and the $SnO_2(110)$ direction, respectively. The interatomic distances in the lattice contrast profiles obtained by 0.2 nm electron-beam scanning were estimated to be 0.194, 0.198, and 0.334 nm for $Pt_3Co(200)$, Pt(200), and $SnO_2(110)$ planes, respectively. The TEM images for the as-fabricated $SnO_2/Pt_3Co/C$ in Figure 3c revealed the Pt-enriched-surface Pt_3Co nanoparticles with 2−3 Pt surface layers, similar to the case of a Pt_3Co/C sample.[8,17,24] These results indicate that the SnO_2 nanoislands on the Pt skin in the as-fabricated $SnO_2/Pt_3Co/C$ sample did not break the geometric feature of the Pt shell/Pt_3Co core structure.

Electrochemical and Material Properties of the Nano-$SnO_2/Pt_3Co/C$. The electrochemical properties of the $SnO_2/Pt_3Co/C$ catalysts with different Pt/Sn ratios after the aging were measured at RDE in 0.1 M $HClO_4$. Typical CV curves for $SnO_2/Pt_3Co/C$ (Pt/Sn = 9/1) and Pt_3Co/C, respectively, after the aging (ADT 0 cycle) and ADT 1000−5000 cycles are shown in Figure 4a,b. The electrochemical surface areas (ECSAs) of the catalysts estimated from the hydrogen adsorption and desorption peak areas in the CVs of Figures 4 and S5 are shown in Figure 4c. The addition of a small amount of Sn to Pt_3Co/C (Pt/Sn = 11/1) showed a slight increase in the ECSA, and more Sn addition (Pt/Sn = 9/1) increased the ECSA twofold compared to that of the Pt_3Co/C, though their particle sizes are similar. The ECSA decreased a little by further Sn addition (Pt/Sn = 4/1) because of increasing physical block of the nano-SnO_2.

Figure 5a,c are the HR-TEM images of the Pt_3Co/C and $SnO_2/Pt_3Co/C$ (Pt/Sn = 9/1), respectively, after the aging and show the atomic arrangements of typical (111) planes of Pt_3Co nanoparticles. The lattice contrast profiles of Figure 5b along the red and blue arrows in Figure 5a for a Pt_3Co/C particle revealed the regular $Pt_3Co(220)$ interplane distance (0.195 nm) for the Pt_3Co core and the Pt(220) interplane distances (two sorts of distances 0.196 and 0.199 nm) for the three surface layers, indicating heterogeneous Pt arrangements at the surface after the aging treatment.

The HR-TEM image for the $SnO_2/Pt_3Co/C$ (Pt/Sn = 9/1) after the aging in Figure 5c showed that the Pt-enriched surface typically possessed many atomic defects and dislocations compared to the Pt_3Co/C surface as indicated by yellow arrows. The lattice contrast profiles in Figures 5d and S6 along the red, blue, and green arrows near the defects and dislocations (labeled a−e) in Figure 5c showed the irregular intensities and intervals, which evidence a rough/skeleton surface morphology at the Pt surface layers. The atomic arrangements averaged with 10 surface atoms showed totally the 0.194−0.195 nm interplane distances, indicating that the compressive strain at the Pt surface layers is due to the effect of the underlying Pt_3Co core structure with the lattice distance shorter than that for pure Pt. The surface also involved less compressive areas with a 0.198 nm interplane distance, indicating an inhomogeneous aspect of the Pt skeleton surface (Figures S7 and S8).
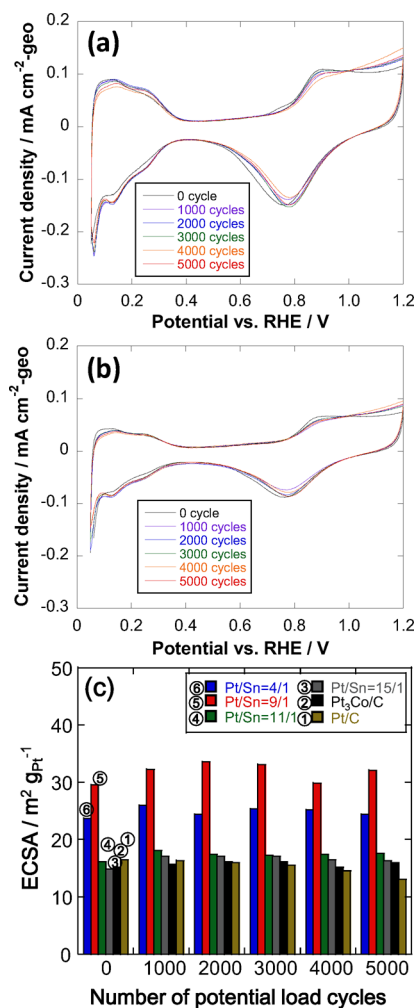

Figure 4. Typical CV curves for (a) $SnO_2/Pt_3Co/C$ (Pt/Sn = 9/1) and (b) Pt_3Co/C. (c) Electrochemical surface areas (ECSA) of the catalysts estimated from the hydrogen adsorption and desorption peak areas in the CVs of Figure S4.

Figure 5e shows a TEM image of the $SnO_2/Pt_3Co/C$ catalyst (Pt/Sn = 9/1) (same particle as that in Figure 5c), and Figure 5f shows EDS line profiles for Pt (blue), Co (red), and Sn (green) along the light blue line of the TEM image, showing the Pt-enriched surface with SnO_2 nanoislands. The surface inhomogeneity may be partially due to heterogeneous distribution of SnO_2 nanoislands with approximately 0.4−1.3 nm dimension at the Pt surface as shown in the EDS profile of Figure 5f. The electrochemical Sn deposition on the Pt-skin surface of Pt_3Co nanoparticles at the potential of −0.45 V vs Ag/AgCl induces surface Pt−Sn alloy formation as well as simple Sn adsorption, and the subsequent surface oxidation of the adsorbed Sn atoms at the surface and the alloyed Sn atoms in the surface layers to form SnO_2 nanoislands should make the surface layers rougher. Furthermore, the leaching of the remaining Sn^0 atoms and a portion the of Co^0 atoms in the Pt_3Co nanoparticles by the aging treatments in the voltage range of 0.05−1.2 V_{RHE} at 50 mV s^{-1} in 0.1 M $HClO_4$ leaves many defects and dislocations behind after their removal and enhances the formation of a rough skeleton surface with increasing ECSAs as illustrated in Figure 5g. The ECSAs of the $SnO_2/Pt_3Co/C$ (Pt/Sn = 4/1, 9/1, and 11/1) did not decrease until ADT 5000 load cycles (Figure 4c), showing high stability,
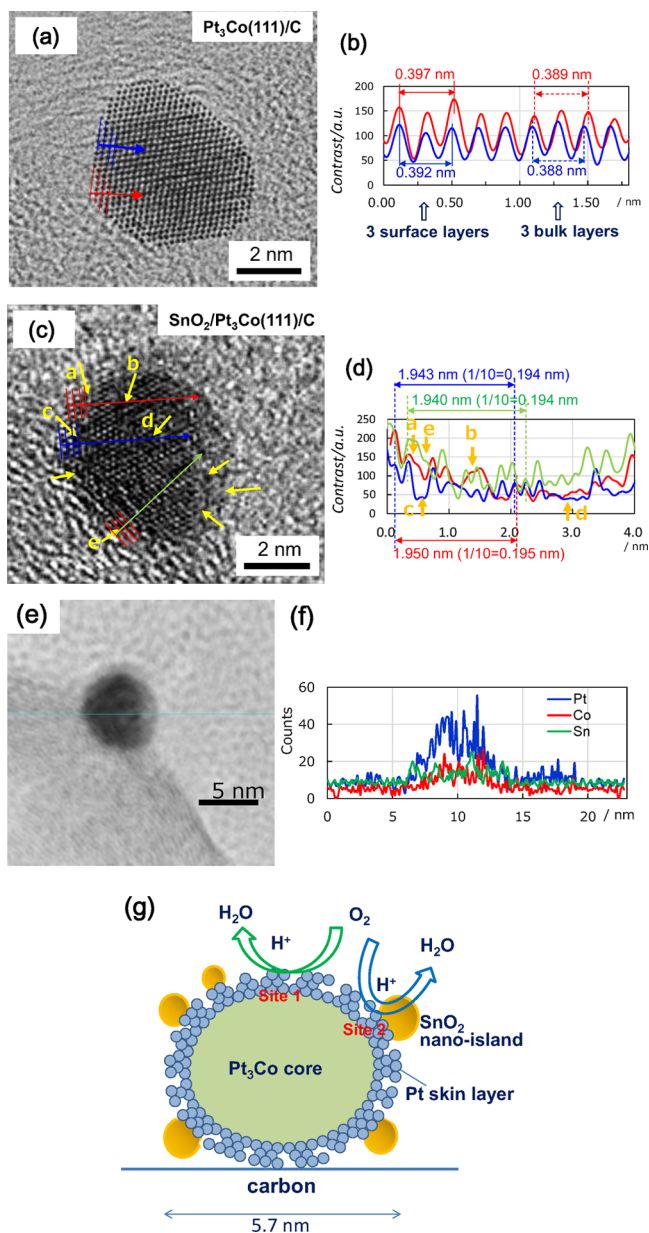
Figure 5. (a) Atomic arrangement of $Pt_3Co(111)$ plane in a TEM image of the Pt_3Co/C after the aging. (b) Lattice contrast profiles for the interplane distances along the red and blue arrows of a: Interplane distances are around 0.195 nm in the $Pt_3Co(220)$ direction and around 0.199 nm in the $Pt(220)$ direction. (c) Atomic arrangement of $Pt_3Co(111)$ plane in a TEM image of the $SnO_2/Pt_3Co/C$ (Pt/Sn = 9/1) after aging. Yellow arrows show typical defects and dislocations. (d) Lattice contrast profiles for the interplane distances along the red and blue arrows of c, showing surface skeleton arrangements with defects and dislocations of Pt atoms; the 10-interplanes distance corresponds to 0.195 nm for the $Pt_3Co(220)$ direction. (e) TEM image of the $SnO_2/Pt_3Co/C$ catalyst (Pt/Sn = 9/1) (same particle as c) and (f) EDS line profiles for Pt (blue), Co (red), and Sn (green) along the light blue line of the TEM image, showing the Pt-enriched surface with SnO_2 nanoislands. (g) Model structure and proposed ORR sites (sites 1 and 2) for the nano-SnO_2-decorated Pt_3Co/C with Pt skeleton surface with compressive strain and defects/dislocations.

whereas the ECSA of the Pt/C catalyst with the similar Pt particle size decreased with ADT cycles (Figure 4c).

Performance Promotion by the Nano-SnO_2. ORR activities of the fabricated cathode catalysts were estimated by

LSV at 0.9 V_{RHE} (Figures 6a,b and S9), and mass activities (MAs) and surface specific activities (SAs) for the SnO_2/
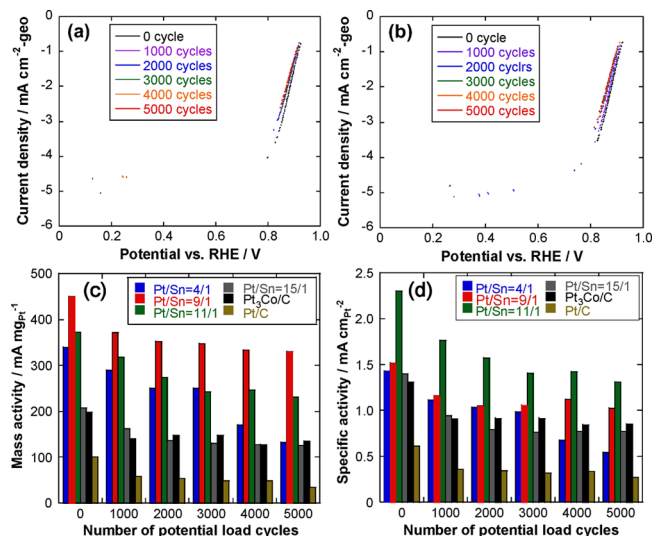

Figure 6. (a and b) Typical LSV curves at 1600 rpm for the $SnO_2/Pt_3Co/C$ catalyst with Pt/Sn = 9/1 and 11/1, respectively, after the ADT 0−5000 cycles at RDE (4.4 μg-Pt cm^{-2}) in 0.1 M $HClO_4$. (c and d) Mass activities (MA) and surface-specific activities (SA), respectively, at 0.9 V_{RHE} for the $SnO_2/Pt_3Co/C$ with Pt/Sn = 4/1, 9/1, 11/1, and 15/1), Pt_3Co/C, and Pt/C. ECSA, MA, and SA values for 10 000 load cycles are shown in Figure S10.

Pt_3Co/C (Pt/Sn = 4/1, 9/1, 11/1, and 15/1), Pt_3Co/C, and Pt/C catalysts were estimated by the Koutecky−Levich plots calculated from the LSV curves as shown in Figure 6c,d, respectively. The MA of the Pt_3Co/C was 2.2 times larger than that of Pt/C, which is among the MA values in the literature.[8,11,13,15,19] It should be noted that the MA of the Pt_3Co/C was increased a further 2.4 times by SnO_2 addition (Pt/Sn = 9/1). Thus, the MA of the $SnO_2/Pt_3Co/C$ catalyst (Pt/Sn = 9/1) was 5.4 times larger than that of the Pt/C catalyst. This is in contrast to the fact that similarly fabricated SnO_2 nanoislands in a $SnO_2/Pt/C$ sample without Co did not promote Pt/C performance (Figure S11). The surface atomic arrangement of $SnO_2/Pt/C$ (Pt/Sn = 5/1) did not show any compressive strain though there were defects and dislocations (Figure S12). The advantage of $SnO_2/Pt_3Co/C$ (Pt/Sn = 9/1) was that it was also maintained after 5000 load cycles, where the MA of the $SnO_2/Pt_3Co/C$ was 7.8 times larger than that of the Pt/C, showing the high durability of the $SnO_2/Pt_3Co/C$. Figure 6c reveals that there is an optimum SnO_2 amount for the ORR promotion and the durability improvement.

The highest SA at 0.9 V_{RHE} among the $SnO_2/Pt_3Co/C$ catalysts after aging was observed with the Pt/Sn = 11/1 catalyst as a result of the relatively smaller ECSA as shown in Figure 4c. The SA of the $SnO_2/Pt_3Co/C$ with Pt/Sn = 11/1 after the 5000 load cycles was 5.0 times larger than that of the Pt/C. However, the SA of the Pt/Sn = 4/1 decreased almost linearly with the load cycles. Thus, the MA and SA of the $SnO_2/Pt_3Co/C$ catalysts are most promoted around Pt/Sn = 9−11/1.

Figure 7a,b shows an HR-TEM image and lattice contrast profiles for $SnO_2/Pt_3Co/C$ (Pt/Sn = 9/1) after ADT 5000 load cycles, respectively. Atomic arrangement in $Pt_3Co(111)$ plane and lattice contrast profiles for the $Pt_3Co(220)$ interplane
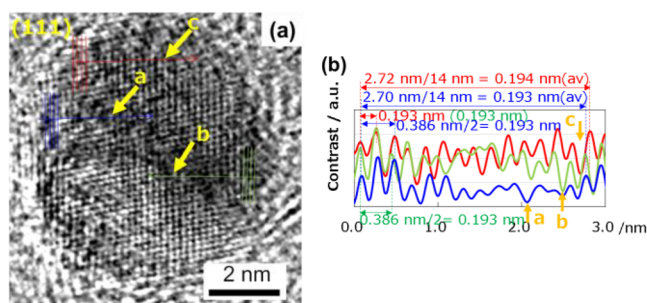
Figure 7. HR-TEM image and lattice contrast profiles for SnO_2/Pt_3Co/C (Pt/Sn = 9/1) after ADT 5000 load cycles. (a) Atomic arrangement of $Pt_3Co(111)$ plane. (b) Lattice contrast profiles for the $Pt_3Co(220)$ interplane distances along the red, blue, and green arrows of a, showing surface skeleton arrangements with defects and dislocations of Pt atoms. Yellow arrows show typical defects and dislocations. The interplane distance around 0.193 nm in the $Pt_3Co(220)$ direction suggests a compressive strain at the Pt-enriched surface.

distances along the red, blue, and green arrows in the TEM image revealed the Pt-enriched skeleton-skin surface with defects and dislocations and with a compressive strain similar to the sample after aging (Figure 5c,d) . The similar images and lattice contrast profiles are also shown in Figure S13. The EDS line profiles for Pt, Co, and Sn in SnO_2/Pt_3Co/C (Pt/Sn = 9/1) after ADT 5000 cycles are also shown in Figure S14. (The aspect is similar to that shown in Figure 5f.) Histograms of particle sizes and average particle sizes for SnO_2/Pt_3Co/C samples (Pt/Sn = 9/1 and 11/1), Pt_3Co/C, and Pt/C after the ADT 5000 cycles estimated from TEM images (Figure S15) indicate that the samples with surface nano-SnO_2 are tolerant to particle growth compared to the samples without SnO_2 nanoislands. This durable property of the SnO_2/Pt_3Co/C samples may bring about their high durability in the ORR performances.

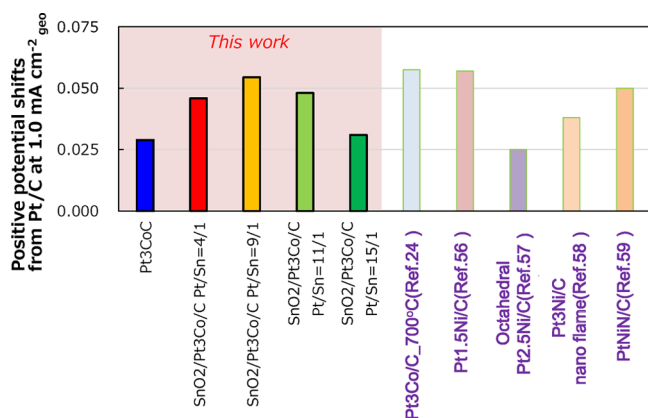Figure 8 shows a comparison of the performances of the nano-SnO_2/Pt_3Co/C catalysts with five representatives of

Figure 8. Comparison of the ORR activities of the nano-SnO_2/Pt_3CO/C with those of five representatives reported to date.

remarkable performances reported to date, where the followings were regarded to be at the highest activity levels: Pt_3Co/C treated at 700 °C,[24] $Pt_{1.5}Ni$/C,[56] octahedral $Pt_{2.5}Ni$/C,[57] nanoflame Pt_3Ni/C,[58] and PtNiN/C.[59] The ORR performances are often presented along with those of standard Pt/C catalysts, but their Pt/C performances are different from

each other in the literature. Hence, for comparison here, we used the positive shifts of the potentials at 1.0 mA/cm^2_{geo} for the examined samples from the potentials of each Pt/C reported at each literature. Figure 8 reveals that the activities of the nano-SnO_2/Pt_3Co/C catalysts with Pt/Sn = 9–11/1 were comparable to those of the top-level samples. Figure 6 also shows the much better durability of the nano-SnO_2/Pt_3Co/C versus that of Pt/C. Thus, the catalyst fabrication method by the selective electrochemical Sn deposition may be promising because the method can be applied to any bimetal systems.

To examine the possibility that the promoting effect of the SnO_2 nanoislands may originate from adjustment of the d-band center of the catalysts, we have measured CO-stripping potentials. The CO-stripping potentials at Pt and Pt-alloy nanoparticle surfaces correlate directly with Pt d-band center.[60−63] The CO-stripping potential peaks for Pt/C and Pt_3Co/C were observed at 800−900 mV as shown in Figure 9a. As for SnO_2/Pt_3Co/C with Pt/Sn = 15/1, 11/1, 9/1, and 4/1, the new peaks at the lower potentials in addition to the 800−900 mV peaks were also observed as discussed below. The surface sites for the 800−900 mV peaks are assigned as site 1 at the Pt surface in Figure 5g. The SAs of the catalysts were plotted against the CO-stripping peak potentials in Figure 9b, which changed as follows: Pt/C < Pt_3Co/C < SnO_2/Pt_3Co/C (Pt/Sn = 15/1) < SnO_2/Pt_3Co/C (Pt/Sn = 11/1) > SnO_2/Pt_3Co/C (Pt/Sn = 9/1) > SnO_2/Pt_3Co/C (Pt/Sn = 4/1), resulting in the volcano relationship between the CO-stripping peak potentials (relative d-band centers) and the SAs as shown in Figure 9b. The SAs of Pt-alloy catalysts have also been demonstrated to reveal a volcano relationship with their d-band center energies as shown by the green dotted line of Figure 9b, where the two values reported in the literature[20,34] for each (1) Pt/C, (2) Pt_3Ni/C, (3) Pt_3Co/C, (4) Pt_3Fe/C, (5) Pt_3V/C, and (6) Pt_3Ti/C were averaged and the values for the Pt_3Co/C and Pt/C were normalized to the CO-stripping peak potentials measured in this study for comparison. Thus, we note that the nano-SnO_2 in the SnO_2/Pt_3Co/C with a compressive strain at the Pt skeleton surface layers electronically modified the 5d level to decrease the d-band center, which leads to weaker oxygen adsorption and improvement of the ORR.

However, the same d-band center value did not show the same ORR activity (Figure 9b), which indicates the existence of another factor for the ORR promotion in case of the SnO_2/Pt_3Co/C catalysts in addition to the appropriate adjustment of d-band center at the Pt surface sites (site 1). The additional CO-stripping peaks at the much lower potentials (700−800 mV) appeared with the nano-SnO_2-decorated catalysts (Figure 9a), which are regarded as due to the event at new surface sites (site 2). The redox change of SnO_2 cannot be responsible for the promotion because of preferable Sn^{4+} states in the range 0.4−1.0 V_{RHE} from the redox potential of Sn atoms. Thus, we propose that the periphery sites of the SnO_2 nanoislands with proton affinity at the Pt skeleton surface may provide the lower potential CO-stripping sites and hence new ORR sites (site 2 in Figure 5g) for more weakly adsorbed O_2, facilitating the H^+−O_2 interaction.

To obtain the electronic and structural information on the nano-SnO_2/Pt_3Co/C catalysts, we conducted in situ XAFS measurements at RDE in 0.1 M $HClO_4$ by using a homemade in situ XAFS cell (Figure S16). Figure S17 shows the change in the peak height of the white line (2p → 5d) in in situ Pt L_{III}-edge XANES spectra of the Pt/C, Pt_3Co/C, and SnO_2/Pt_3Co/C under the stepwise potential operations 0.4 V → 0.6 V → 0.8
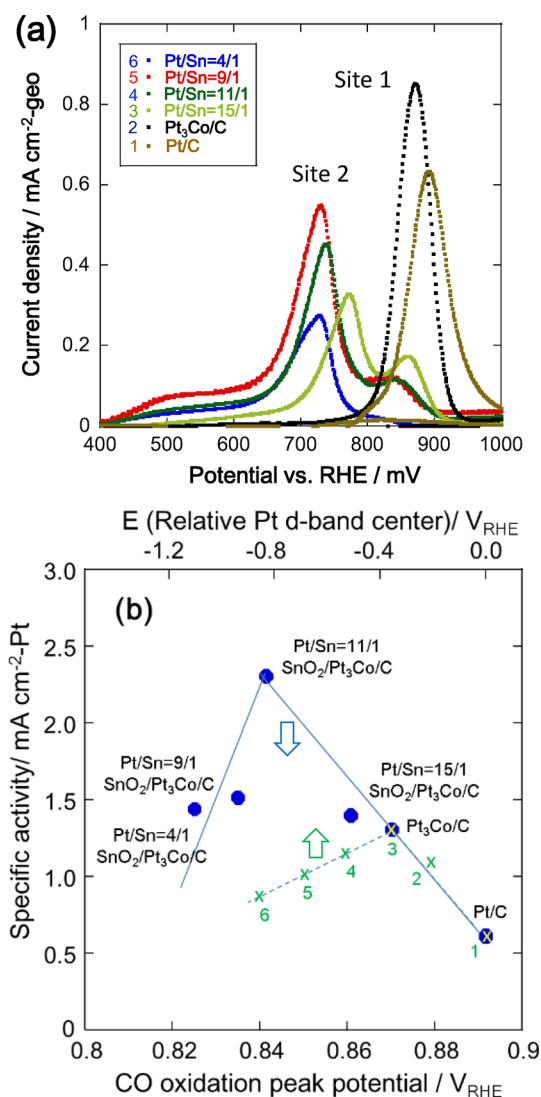
(a)

(b)

Figure 9. (a) CO-stripping peak potentials for (1) Pt/C, (2) Pt$_3$Co/C, and (3−6) SnO$_2$/Pt$_3$Co/C with Pt/Sn = 15/1, 11/1, 9/1, and 4/1, respectively. (b) Correlation between the specific activity (SA) and the CO-stripping peak potentials for the SnO$_2$/Pt$_3$Co/C (Pt/Sn = 4/1, 9/1, 11/1, and 15/1), Pt$_3$Co/C, and Pt/C. The green dotted line represents averaged from the data of refs 20 and 34 for (1) Pt/C, (2) Pt$_3$Ni/C, (3) Pt$_3$Co/C, (4) Pt$_3$Fe/C, (5) Pt$_3$V/C, and (6) Pt$_3$Ti/C, also shown by scaling of the relative d-band center, where the values of Pt/C and Pt$_3$Co/C (yellow ×'s over blue dots) from refs 20 and 34 were normalized to the values in the present study.

V → 1.0 V → 0.8 V → 0.6 V → 0.4 V vs RHE at RDE in 0.1 M HClO$_4$. The white line peak intensity reflects the degree of the vacancy of Pt 5d orbitals near the Fermi level. In the potential gain processes from 0.4 to 1.0 V$_{RHE}$, the catalysts showed an increase of the white line intensity above 0.8 V$_{RHE}$ (Figure 10), indicating a positive charge of the Pt surfaces due to Pt−O bonding.[64] In the potential down processes from 1.0 to 0.4 V$_{RHE}$, the white line responses for the Pt/C and Pt$_3$Co/C did not retrace those in the potential gain processes, showing a definite hysteresis. It is notable that nano-SnO$_2$/Pt$_3$Co/C exhibited no hysteresis in the potential operations between 0.4 and 1.0 V$_{RHE}$. Oxygen species adsorbed on the SnO$_2$/Pt$_3$Co/C surface at 1.0 V$_{RHE}$ are readily reduced below 1.0 V$_{RHE}$, resulting in the higher ORR performance. The in situ Co K-edge XANES spectra analysis for SnO$_2$/Pt$_3$Co/C (Pt/Sn = 11/
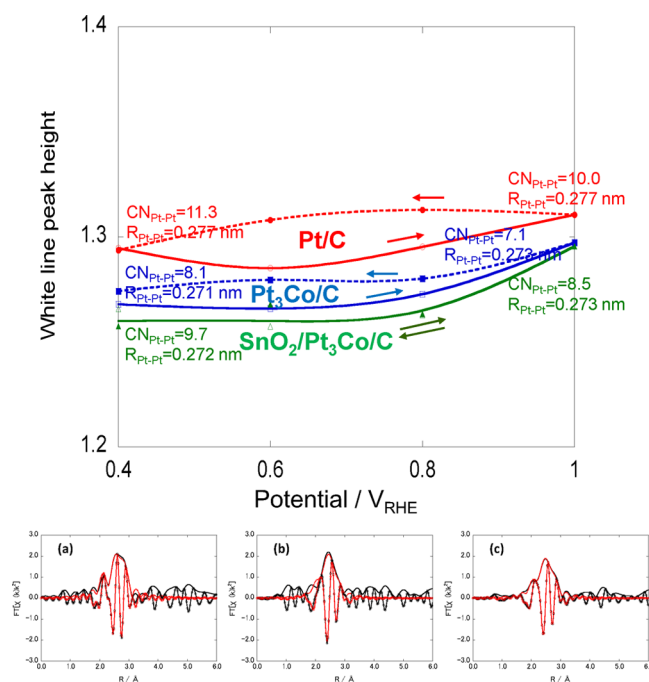

Figure 10. (top) White line peak heights in the XANES spectra for Pt/C (red), Pt$_3$Co/C (blue), and SnO$_2$/Pt$_3$Co/C with Pt/Sn = 11/1 (green) in the potential gain and down processes every 0.2 V between 0.4 and 1.0 V$_{RHE}$. CN$_{Pt−Pt}$ and R$_{Pt−Pt}$ are coordination numbers and bond distances, respectively, for Pt−Pt at 0.4 and 1.0 V$_{RHE}$ (Table S1 and Figures S15−17). (bottom) EXAFS Fourier transforms and curve-fittings for (a) Pt/C, (b) Pt$_3$Co/C, and (c) SnO$_2$/Pt$_3$Co/C (Pt/Sn = 11/1) at 0.4 V$_{RHE}$.

1) in the potential operations revealed no change in the Co states of the Pt$_3$Co core (Figure S18). In-situ Sn K-edge XANES spectra with good quality in the potential operations could not be tracked, but our previous study for the MEA Pt−Sn(oxidized)/C samples evidenced no change in the Sn states in 200 I−V load cycles, indicating a high stability under the PEFC operating conditions.[37] Ex situ XAFS spectra at Pt L$_{III}$-edge, Co K-edge, and Sn K-edge for SnO$_2$/Pt$_3$Co/C samples (Pt/Sn = 9/1 and 11/1) after aging and ADT 5000 cycles could be observed, and those data are shown in Figure S19. The ex situ XANES spectra and EXAFS oscillations and Fourier transforms at Pt L$_{III}$-edge, Co K-edge, and Sn K-edge after aging and ADT 5000 cycles, respectively, did not change, which suggests that the electronic states and local structures of Pt, Co, and Sn atoms in the SnO$_2$/Pt$_3$Co/C samples remained unchanged after the ADT 5000 load cycles. These data also reveal the high durability of the SnO$_2$/Pt$_3$Co/C samples under the PEFC operating conditions.

The compressive strain at the Pt surface layers was also suggested by the shorter Pt−Pt bond distances (0.271−0.272 nm) for the Pt$_3$Co/C and SnO$_2$/Pt$_3$Co/C catalysts compared to 0.277 nm for the Pt/C catalyst with the similar Pt nanoparticle size (Figure 10a−c and Table S1), which were decided by the in situ EXAFS curve-fitting analysis in Figures 10a−c and S20−22. The oxygen adsorption at 1.0 V$_{RHE}$ caused the decrease in the coordination number of Pt−Pt bonds probably because of the distorted rearrangement of Pt atoms at the topmost layer by the Pt−O bonding. The ORR promotion by the SnO$_2$ nanoislands decoration is not referred to the downshift of the d-band center for the Pt skeleton layers (site 1) because too much reduction of the d-band center level

decreases the SAs for Pt$_3$V/C and Pt$_3$Ti/C (Figure 9b) but rather to the new reactive periphery sites (site 2) of the SnO$_2$ nanoislands at the Pt skeleton surface (Figure 5g). The ECSA of the periphery sites is not clear at moment because the CO adsorption cannot simply be compared to the hydrogen adsorption in the case of the rough skeleton surface, but if the periphery area (site 2) is provisionally one-third or -half, respectively, of the ECSA, then the SA of site 2 in the SnO$_2$/Pt$_3$Co/C with Pt/Sn = 11/1 is estimated to be 7.8 or 5.2 times larger than the SA of site 1 expected from the d-band center value.

CONCLUSIONS

The significant improvements for the ORR activity and durability were achieved with the new nano-SnO$_2$/Pt$_3$Co/C catalysts, which were regulated by a strategic fabrication using a new selective electrochemical Sn deposition method and subsequent chemical treatments. The nano-SnO$_2$/Pt$_3$Co/C catalysts with Pt/Sn = 9/1 and 11/1 were among the samples with the highest performance levels reported to date. The nano-SnO$_2$/Pt$_3$Co/C catalysts after the aging treatments possessed a Pt$_3$Co core/Pt skeleton-skin structure decorated with SnO$_2$ nanoislands at the surface. Their high performances originated from the unique reactive periphery sites of the SnO$_2$ nanoislands at the compressive Pt skeleton surface (Pt–Pt distance = 0.272 nm) with the defects and dislocations in addition to the compressive Pt skin surface. The ORR activity and durability of Pt$_3$Co/C were tuned by changing the amount of surface SnO$_2$ nanoislands. The white line peak intensity of nano-SnO$_2$/Pt$_3$Co/C revealed no hysteresis in the potential up–down operations between 0.4 and 1.0 V$_{RHE}$, unlike the cases of Pt/C and Pt$_3$Co/C, indicating weaker oxygen adsorption and higher ORR activity compared to those of Pt/C and Pt$_3$Co/C. The present results provide a new insight into development of a new class of next-generation PEFC cathode catalysts with two different active sites.

ASSOCIATED CONTENT

Ⓢ Supporting Information

The Supporting Information is available free of charge on the ACS Publications website at DOI: 10.1021/jacs.5b04256.

XRD, XPS, STEM, lattice contrast profiles, CV, LSV curves, XANES, and EXAFS data and in situ XAFS setup. (PDF)

AUTHOR INFORMATION

Corresponding Author
*iwasawa@pc.uec.ac.jp

Notes
The authors declare no competing financial interest.

ACKNOWLEDGMENTS

REFERENCES

(1) Debe, M. K. Nature 2012, 486, 43–51.

(2) Rabis, A.; Rodriguez, P.; Schmidt, T. J. ACS Catal. 2012, 2, 864–890.

(3) Wu, G.; More, K. L.; Johnston, C. M.; Zelenay, P. Science 2011, 332, 443–447.

(4) Borup, R.; Meyers, J.; Pivovar, B.; Kim, Y. S.; Mukundan, R.; Garland, N.; Myers, D.; Wilson, M.; Garzon, F.; Wood, D.; Zelenay, P.; More, K.; Stroh, K.; Zawodzinski, T.; Boncella, J.; McGrath, J. E.; Inaba, M.; Miyatake, K.; Hori, M.; Ota, K.; Ogumi, Z.; Miyata, S.; Nishikata, A.; Siroma, Z.; Uchimoto, Y.; Yasuda, K.; Kimijima, K.; Iwashita, N. Chem. Rev. 2007, 107, 3904–3951.

(5) Stamenkovic, V. R.; Fowler, B.; Mun, B. S.; Wang, G.; Ross, P. N.; Lucas, C. A.; Markovic, N. M. Science 2007, 315, 493–497.

(6) Strasser, P.; Koh, S.; Anniyev, T.; Greeley, J.; More, K.; Yu, C.; Liu, Z.; Kaya, S.; Nordlund, D.; Ogasawara, H.; Toney, M. F.; Nilsson, A. Nat. Chem. 2010, 2, 454–460.

(7) Wu, J.; Yang, H. Acc. Chem. Res. 2013, 46, 1848–1857.

(8) Xin, H. L.; Mundy, J. A.; Liu, Z.; Cabezas, R.; Hovden, R.; Kourkoutis, L. F.; Zhang, J.; Subramanian, N. P.; Makharia, R.; Wagner, F. T.; Muller, D. A. Nano Lett. 2012, 12, 490–497.

(9) Ohkubo, Y.; Hamaguchi, Y.; Seino, S.; Nakagawa, T.; Kageyama, S.; Kugai, J.; Nitani, H.; Ueno, K.; Yamamoto, T. J. Mater. Sci. 2013, 48, 5047–5054.

(10) Greeley, J.; Stephens, I. E. L.; Bondarenko, A. S.; Johansson, T. P.; Hansen, H. A.; Jaramillo, T. F.; Rossmeisl, J.; Chorkendorff, I.; Nørskov, J. K. Nat. Chem. 2009, 1, 552–556.

(11) Koh, S.; Strasser, P. J. Am. Chem. Soc. 2007, 129, 12624–12625.

(12) Toda, T.; Igarashi, H.; Uchida, H.; Watanabe, M. J. Electrochem. Soc. 1999, 146, 3750–3756.

(13) Loukrakpam, R.; Luo, J.; He, T.; Chen, Y. S.; Xu, Z.; Njoki, P. N.; Wanjala, B. N.; Fang, B.; Mott, D.; Yin, J.; Klar, J.; Powell, B.; Zhong, C. J. Phys. Chem. C 2011, 115, 1682–1694.

(14) Mani, P.; Srivastava, R.; Strasser, P. J. Power Sources 2011, 196, 666–674.

(15) Paulus, U. A.; Wokaun, A.; Scherer, G. G.; Schmidt, T. J.; Stamenkovic, V.; Radmilovic, V.; Markovic, N. M.; Ross, P. N. J. Phys. Chem. B 2002, 106, 4181–4191.

(16) Chen, S.; Gasteiger, H. A.; Hayakawa, K.; Tada, T.; Shao-Horn, Y. J. Electrochem. Soc. 2010, 157, A82–A97.

(17) Chen, S.; Sheng, W.; Yabuuchi, N.; Ferreira, P. J.; Allard, L. F.; Shao-Horn, Y. J. Phys. Chem. C 2009, 113, 1109–1125.

(18) Salvatore Aricò, A.; Stassi, A.; Gatto, I.; Monforte, G.; Passalacqua, E.; Antonucci, V. J. Phys. Chem. C 2010, 114, 15823–15836.

(19) Wang, C.; Chi, M.; Li, D.; Strmcnik, D.; van der Vliet, D.; Wang, G.; Komanicky, V.; Chang, K.; Paulikas, A. P.; Tripkovic, D.; Pearson, J.; More, K. L.; Markovic, N. M.; Stamenkovic, V. R. J. Am. Chem. Soc. 2011, 133, 14396–14403.

(20) Stamenkovic, V. R.; Mun, B. S.; Arenz, M.; Mayrhofer, K. J. J.; Lucas, C. A.; Wang, G.; Ross, P. N.; Markovic, N. M. Nat. Mater. 2007, 6, 241–247.

(21) Mukerjee, S.; Srinivasan, S.; Soriaga, M. P.; Mcbreen, J. J. Phys. Chem. 1995, 99, 4577–4589.

(22) Carlton, C. E.; Chen, S.; Ferreira, P. J.; Allard, L. F.; Shao-Horn, Y. J. Phys. Chem. Lett. 2012, 3, 161–166.

(23) Wang, C.; Markovic, N. M.; Stamenkovic, V. R. ACS Catal. 2012, 2, 891–898.

(24) Wang, D.; Xin, H. L.; Hovden, R.; Wang, H.; Yu, Y.; Muller, D. A.; DiSalvo, F. J.; Abruña, H. D. Nat. Mater. 2012, 12, 81–87.

(25) Xin, H. L.; Mundy, J. A.; Liu, Z.; Cabezas, R.; Hovden, R.; Kourkoutis, L. F.; Zhang, J.; Subramanian, N. P.; Makharia, R.; Wagner, F. T.; Muller, D. A. Nano Lett. 2012, 12, 490–497.

(26) Durst, J.; Lopez-Haro, M.; Dubau, L.; Chatenet, M.; Soldo-Olivier, Y.; Guetaz, L.; Bayle-Guillemaud, P.; Maillard, F. J. Phys. Chem. Lett. 2014, 5, 434–439.

(27) Yu, Y.; Xin, H. L.; Hovden, R.; Wang, D.; Rus, E. D.; Mundy, J. A.; Muller, D. A.; Abruna, H. Nano Lett. 2012, 12, 4417–4423.

(28) Heggen, M.; Oezaslan, M.; Houben, L.; Strasser, P. J. Phys. Chem. C 2012, 116, 19073–19083.

(29) Tada, M.; Murata, S.; Asakoka, T.; Hiroshima, K.; Okumura, K.; Tanida, H.; Uruga, T.; Nakanishi, H.; Matsumoto, S.; Inada, Y.; Nomura, M.; Iwasawa, Y. *Angew. Chem., Int. Ed.* **2007**, *46*, 4310−4315.

(30) Ishiguro, N.; Saida, T.; Uruga, T.; Nagamatsu, S.; Sekizawa, O.; Nitta, K.; Yamamoto, T.; Ohkoshi, S.; Iwasawa, Y.; Yokoyama, T.; Tada, M. *ACS Catal.* **2012**, *2*, 1319−1330.

(31) Ishiguro, N.; Kityakarn, S.; Sekizawa, O.; Uruga, T.; Sasabe, T.; Nagasawa, K.; Yokoyama, T.; Tada, M. *J. Phys. Chem. C* **2014**, *118*, 15874−15883.

(32) Saida, T.; Sekizawa, O.; Ishiguro, N.; Hoshino, M.; Uesugi, K.; Uruga, T.; Ohkoshi, S.; Yokoyama, T.; Tada, M. *Angew. Chem., Int. Ed.* **2012**, *51*, 10311−10314.

(33) Takao, S.; Sekizawa, O.; Nagamatsu, S.; Kaneko, T.; Yamamoto, T.; Samjeské, G.; Higashi, K.; Nagasawa, K.; Tsuji, T.; Suzuki, M.; Kawamura, N.; Mizumaki, M.; Uruga, T.; Iwasawa, Y. *Angew. Chem., Int. Ed.* **2014**, *53*, 14110−14114.

(34) Stamenkovic, V. R.; Mun, B. S.; Mayrhofer, K. J. J.; Ross, P. N.; Markovic, N. M.; Rossmeisl, J.; Greeley, J.; Nørskov, J. K. *Angew. Chem., Int. Ed.* **2006**, *45*, 2897−2901.

(35) Matanovic, I.; Garzon, F. H.; Henson, N. J. *J. Phys. Chem. C* **2011**, *115*, 10640−10650.

(36) Friebel, D.; Viswanathan, V.; Miller, D. J.; Anniyev, T.; Ogasawara, H.; Larsen, A. H.; O'Grady, C. P.; Nørskov, J. K.; Nilsson, A. *J. Am. Chem. Soc.* **2012**, *134*, 9664−9671.

(37) Samjeské, G.; Nagamatsu, S.; Takao, S.; Nagasawa, K.; Imaizumi, Y.; Sekizawa, O.; Yamamoto, T.; Uemura, Y.; Uruga, T.; Iwasawa, Y. *Phys. Chem. Chem. Phys.* **2013**, *15*, 17208−17218.

(38) Samjeské, G.; Nagamatsu, S.; Nagasawa, K.; Imaizumi, Y.; Takao, S.; Sekizawa, O.; Yamamoto, T.; Uruga, T.; Iwasawa, Y. *ECS Trans.* **2013**, *50*, 1651−1657.

(39) Uemura, Y.; Inada, Y.; Bando, K. K.; Sasaki, T.; Kamiuchi, N.; Eguchi, K.; Yagishita, A.; Nomura, M.; Tada, M.; Iwasawa, Y. *J. Phys. Chem. C* **2011**, *115*, 5823−5833.

(40) Uemura, Y.; Inada, Y.; Bando, K. K.; Sasaki, T.; Kamiuchi, N.; Eguchi, K.; Yagishita, A.; Nomura, M.; Tada, M.; Iwasawa, Y. *Phys. Chem. Chem. Phys.* **2011**, *13*, 15833−15844.

(41) Ioroi, T.; Fujiwara, N.; Siroma, Z.; Yasuda, K.; Miyazaki, Y. *Electrochem. Commun.* **2002**, *4*, 442−446.

(42) Masuda, T.; Fukumitsu, H.; Fugane, K.; Togasaki, H.; Matsumura, D.; Tamura, K.; Nishihata, Y.; Yoshikawa, H.; Kobayashi, K.; Mori, T.; Uosaki, K. *J. Phys. Chem. C* **2012**, *116*, 10098−10102.

(43) Selvaganesh, S. V.; Selvarani, G.; Sridhar, P.; Pitchumani, S.; Shukla, A. K. *J. Electrochem. Soc.* **2010**, *157*, B1000−B1007.

(44) Ho, V. T. T.; Pan, C. J.; Rick, J.; Su, W. N.; Hwang, B. J. *J. Am. Chem. Soc.* **2011**, *133*, 11716−11724.

(45) Sasaki, K.; Takasaki, F.; Noda, Z.; Hayashi, S.; Shiratori, Y.; Ito, K. *ECS Trans.* **2010**, *33*, 473−482.

(46) Newville, M.; Ravel, B.; Haskel, D.; Rehr, J. J.; Stern, E. A.; Yacoby, Y. *Phys. B* **1995**, *208-209*, 154−156.

(47) Ravel, B.; Newville, M. *J. Synchrotron Radiat.* **2005**, *12*, 537−541.

(48) Ankudinov, A. L.; Ravel, B.; Rehr, J. J.; Conradson, S. D. *Phys. Rev. B: Condens. Matter Mater. Phys.* **1998**, *58*, 7565.

(49) Pozio, A.; De Francesco, M.; Cemmi, A.; Cardellini, F.; Giorgi, L. *J. Power Sources* **2002**, *105*, 13−19.

(50) Shao, Y.; Yin, G.; Gao, Y.; Shi, P. *J. Electrochem. Soc.* **2006**, *153*, A1093−A1097.

(51) Zhang, G.; Zhao, D.; Feng, Y.; Zhang, B.; Su, D.; Liu, G.; Xu, Q. *ACS Nano* **2012**, *6*, 2226−2236.

(52) Wang, K.; Gasteiger, H. A.; Markovic, N. M.; Ross, P. N. *Electrochim. Acta* **1996**, *41*, 2587−2593.

(53) Stamenković, V.; Arenz, M.; Blizanac, B. B.; Mayrhofer, K. J. J.; Ross, P. N.; Marković, N. M. *Surf. Sci.* **2005**, *576*, 145−157.

(54) Liu, P.; Logadottir, A.; Nørskov, J. K. *Electrochim. Acta* **2003**, *48*, 3731−3742.

(55) Lin, W. F.; Zei, M. S.; Eiswirth, M.; Ertl, G.; Iwasita, T.; Vielstich, W. *J. Phys. Chem. B* **1999**, *103*, 6968−6977.

(56) Cui, C.; Gan, L.; Heggen, M.; Rudi, S.; Strasser, P. *Nat. Mater.* **2013**, *12*, 765−771.

(57) Choi, S.; Xie, S.; Shao, M.; Odell, J. H.; Lu, N.; Peng, H.; Protsailo, L.; Guerrero, S.; Park, J.; Xia, X.; Wang, J.; Kim, M. J.; Xia, Y. *Nano Lett.* **2013**, *13*, 3420−3425.

(58) Chen, C.; Kang, Y.; Huo, Z.; Zhu, Z.; Huang, W.; Xin, H. L.; Snyder, J. D.; Li, D.; Herron, J. A.; Mavrikakis, M.; Chi, M.; More, K. L.; Li, Y.; Markovic, N. M.; Somorjai, G. A.; Yang, P.; Stamenkovic, V. R. *Science* **2014**, *343*, 1339−1343.

(59) Kuttiyiel, K. A.; Sasaki, K.; Choi, Y. M.; Su, D.; Liu, P.; Adzic, R. R. *Nano Lett.* **2012**, *12*, 6266−6271.

(60) Hammer, B.; Nørskov, J. K. *Adv. Catal.* **2000**, *45*, 71−129.

(61) Mavrikakis, N. M.; Hammer, B.; Nørskov, J. K. *Phys. Rev. Lett.* **1998**, *81*, 2819−2822.

(62) Stephens, I. E. L.; Bondarenko, A. S.; Grønbjerg, U.; Rossmeisl, J.; Chorkendorff, I. *Energy Environ. Sci.* **2012**, *5*, 6744−6762.

(63) Zhang, G. R.; Zhao, D.; Feng, Y. Y.; Zhang, B.; Su, D. S.; Liu, G.; Xu, B. Q. *ACS Nano* **2012**, *6*, 2226−2236.

(64) Nagamatsu, S.; Arai, T.; Yamamoto, M.; Ohkura, T.; Oyanagi, H.; Ishizaka, T.; Kawanami, H.; Uruga, T.; Tada, M.; Iwasawa, Y. *J. Phys. Chem. C* **2013**, *117*, 13094−13107.